AIP | Physics of Plasmas

Radiative shocks produced from spherical cryogenic implosions at the National Ignition Facility

A. Pak, L. Divol, G. Gregori, S. Weber, J. Atherton et al.

Citation: Phys. Plasmas **20**, 056315 (2013); doi: 10.1063/1.4805081
View online: http://dx.doi.org/10.1063/1.4805081
View Table of Contents: http://pop.aip.org/resource/1/PHPAEN/v20/i5
Published by the American Institute of Physics.

Radiative shocks produced from spherical cryogenic implosions at the National Ignition Facility[a)]

A. Pak,[1,b)] L. Divol,[1] G. Gregori,[2] S. Weber,[1] J. Atherton,[1] R. Bennedetti,[1] D. K. Bradley,[1] D. Callahan,[1] D. T. Casey,[1] E. Dewald,[1] T. Döppner,[1] M. J. Edwards,[1] J. A. Frenje,[3] S. Glenn,[1] G. P. Grim,[4] D. Hicks,[1] W. W. Hsing,[1] N. Izumi,[1] O. S. Jones,[1] M. G. Johnson,[3] S. F. Khan,[1] J. D. Kilkenny,[5] J. L. Kline,[4] G. A. Kyrala,[4] J. Lindl,[1] O. L. Landen,[1] S. Le Pape,[1] T. Ma,[1] A. MacPhee,[1] B. J. MacGowan,[1] A. J. MacKinnon,[1] L. Masse,[6] N. B. Meezan,[1] J. D. Moody,[1] R. E. Olson,[7] J. E. Ralph,[1] H. F. Robey,[1] H.-S. Park,[1] B. A. Remington,[1] J. S. Ross,[1] R. Tommasini,[1] R. P. J. Town,[1] V. Smalyuk,[1] S. H. Glenzer,[1] and E. I. Moses[1]
[1]*Lawrence Livermore National Laboratory, Livermore, California 94550, USA*
[2]*Department of Physics, University of Oxford, Parks Road, Oxford OXI 3PU, United Kingdom*
[3]*Massachusetts Institute of Technology Plasma Science and Fusion Center, Cambridge, Massachusetts 02139, USA*
[4]*Los Alamos National Laboratory, Los Alamos, New Mexico 87545, USA*
[5]*General Atoms, San Diego, California 92121, USA*
[6]*CEA/DAM/DIF, F-91297 Arpajon, France*
[7]*Sandia National Laboratories, Albuquerque, New Mexico 87185, USA*

(Received 25 December 2012; accepted 26 March 2013; published online 20 May 2013)

Spherically expanding radiative shock waves have been observed from inertially confined implosion experiments at the National Ignition Facility. In these experiments, a spherical fusion target, initially 2 mm in diameter, is compressed via the pressure induced from the ablation of the outer target surface. At the peak compression of the capsule, x-ray and nuclear diagnostics indicate the formation of a central core, with a radius and ion temperature of $\sim$20 μm and $\sim$ 2 keV, respectively. This central core is surrounded by a cooler compressed shell of deuterium-tritium fuel that has an outer radius of $\sim$40 μm and a density of $>$500 g/cm^3. Using inputs from multiple diagnostics, the peak pressure of the compressed core has been inferred to be of order 100 Gbar for the implosions discussed here. The shock front, initially located at the interface between the high pressure compressed fuel shell and surrounding in-falling low pressure ablator plasma, begins to propagate outwards after peak compression has been reached. Approximately 200 ps after peak compression, a ring of x-ray emission created by the limb-brightening of a spherical shell of shock-heated matter is observed to appear at a radius of $\sim$100 μm. Hydrodynamic simulations, which model the experiment and include radiation transport, indicate that the sudden appearance of this emission occurs as the post-shock material temperature increases and upstream density decreases, over a scale length of $\sim$10 μm, as the shock propagates into the lower density ($\sim$1 g/cc), hot ($\sim$250 eV) plasma that exists at the ablation front. The expansion of the shock-heated matter is temporally and spatially resolved and indicates a shock expansion velocity of $\sim$300 km/s in the laboratory frame. The magnitude and temporal evolution of the luminosity produced from the shock-heated matter was measured at photon energies between 5.9 and 12.4 keV. The observed radial shock expansion, as well as the magnitude and temporal evolution of the luminosity from the shock-heated matter, is consistent with 1-D radiation hydrodynamic simulations. Analytic estimates indicate that the radiation energy flux from the shock-heated matter is of the same order as the in-flowing material energy flux, and suggests that this radiation energy flux modifies the shock front structure. Simulations support these estimates and show the formation of a radiative shock, with a precursor that raises the temperature ahead of the shock front, a sharp μm-scale thick spike in temperature at the shock front, followed by a post-shock cooling layer.
[http://dx.doi.org/10.1063/1.4805081]

I. INTRODUCTION

In a variety of astrophysical phenomena, including supernova remnants, stellar jets, and cataclysmic variable systems, high velocity radiative shock waves are created. X-ray radiation created from these events offers important insight into the composition and physical properties of such systems. In the case of young supernova remnants, the observed spatial variation of x-ray emission has been used to infer the type of stellar progenitor and details of the ejecta distribution and chemical mixing that occur within the remnant.[1] Additionally, the temporal evolution of x-ray emission can be used to infer the interaction of the radiative shock wave with the surrounding circumstellar medium.[2] Creating radiative shocks in the laboratory, where the initial conditions are known and many

[a)]Paper KI3 1, Bull. Am. Phys. Soc. **57**, 198 (2012).
[b)]Invited speaker.

diagnostics can be used to interrogate the shock evolution and x-ray emission over hydrodynamic time scales not obtainable in a single stellar remnant system, can be used to test hypotheses, hydrodynamic modeling and inform our understanding of x-ray emission from young supernova remnants.

The National Ignition Facility[3] (NIF) is a unique scientific resource, as it has the capability to compress matter to unprecedented densities (1000 g/cc), pressures (100 Gbar), and temperatures (10 keV).[4] Matter at such extreme states, such as those created in an inertially confined fusion experiment, is of interest for studying a variety of astrophysical phenomena, including the radiative hydrodynamics of young supernova.[5,6] Laser driven radiative shocks have previously been studied, in a one dimensional geometry in low density (~mg/cc) xenon or argon filled gas tubes, where radiative effects, such as the creation of a radiative precursor, sharp rise in post-shock temperature, and a dense collapsed downstream cooling layer, have been observed.[7–10] In a cylindrical geometry, radiative blast waves have been created in the momentum conserving snow plow regime, in a xenon plasma at a density of 10^{18}–10^{19} atoms/cc, where radaitive cooling was observed to enhance the deceleration of the blast wave.[11–13] In spherical geometry, the hydrodynamic instabilities of Sedov-Taylor blast waves driven into low density xenon and nitrogen gas filled chambers have been studied using shadowgraphy to probe fluctuations in the index of refraction at the shock front.[14] In this work, we present results detailing the creation of a spherically expanding radiative shock wave, produced by an inertially confined fusion experiment at the NIF. The temporal evolution of the expansion of the shock and luminosity from the shock-heated matter are directly measured and found to be in good agreement with radiation hydrodynamic simulations that have been performed using similar amounts of laser energy and initialized to match the inferred stagnation pressure.

The paper is organized as follows. Section II describes the indirect drive inertially confined fusion experimental setup and details the compression of the capsule, the diagnostics, and the measurements that were made to determine the structure, density, temperature, and pressure of the compressed core. A brief physical picture describing the origin of the radiative shock wave and the subsequent x-ray emission is given. Section III presents results from three implosion experiments that show the sudden appearance and subsequent expansion of a spherical radiative shock wave. In Sec. IV, radiative shock waves and the necessary conditions that must exist for such shocks to be created are discussed. These conditions, taken with the observations from Sec. III, are used to show analytically that the shock wave generated in these implosion experiments is indeed radiative. Section V contains results from a radiation hydrodynamic simulation that indicate the formation of a radiative shock wave in these experiments. Simulation results also show the sudden rise in x-ray radiance that is consistent with experimental observations, which occurs as the shock wave expands outwards. Section VI describes in detail the observed x-ray luminosity produced from the radiative shock wave. The magnitude and the temporal evolution of the x-ray luminosity in the simulation are shown to be in general agreement with the observed luminosity. Finally, a summary of the work presented in this paper and a brief outlook towards future work is given in Sec. VII.

II. EXPERIMENTAL SETUP

At the NIF, cryogenic thermonuclear implosion experiments are being performed to create an inertially confined fusion reaction using the indirect drive technique.[15] Figure 1(a) shows the experimental setup of an indirect drive implosion experiment. In this method, lasers are used to irradiate the inside wall of a cylinder, known as a hohlraum. This produces an x-ray flux with a peak radiation temperature of 300 eV that ablates the outer surface of the fusion capsule target, producing the pressure which compresses the target to sufficient densities and temperatures to initiate the fusion reaction. The NIF uses 192 individual laser beams, each of which is at a wavelength of 351 nm, to irradiate the hohlraum, delivering up to 1.9 MJ and 500 TW of total laser energy and power, respectively. As shown in Fig. 1(a), half of the beams are directed into the cylindrical hohlraum through the upper laser entrance hole (LEH), and the other half through the lower LEH.

Figure 1(b) details the dimensions and composition of a spherical fusion capsule target.[16] The capsule has an initial outer radius of ~1 mm and is composed of several layers of plastic (CH) ablator that surround a solid deuterium-tritium (DT) ice layer and is filled with a equimolar 50:50 mixture of DT gas.

As the capsule target is compressed by the ablation pressure, the temperature and density of the central gas filled region increase, forming a hot core in which deuterium and tritium atoms fuse. The solid DT ice layer of the capsule is also compressed and forms a cooler dense shell of DT fuel that surrounds the hot core. In this scheme, α particles created in the hot core deposit their energy in the dense shell, increasing the temperature and igniting the DT fuel leading to a net gain in energy. In current experiments, the neutron yield indicates that not enough α particles are being generated in the compressed hot core to ignite the dense shell of DT fuel. After peak compression has been reached, the hot core and dense shell of DT fuel expand outwards as internal energy is converted back into kinetic energy.

As discussed below, the size of the hot core is determined from the radius of x-ray bremsstrahlung emission. At peak compression, the radius of the hot core is measured to be ~20–30 μm. In conjunction with the spatially and time resolved x-ray measurements of the hot core emission, nuclear diagnostics are used to measure the pressure, temperature, and density within the hot core. These measurements find that at peak compression, several DT implosion experiments have reached core conditions of ~50–150 Gbar, ~2–4 keV, and ~100 g/cm^{-3}.

Two hardened gated x-ray imager (hGXI) diagnostics[17] temporally and spatially resolve the x-ray emission from the compressed hot core over a ~1 ns duration along the polar and equatorial axes (Fig. 1(a)). Each hGXI uses a pinhole array to image the x-ray emission from the hot core onto a four strip gated micro-channel plate (MCP) detector. The

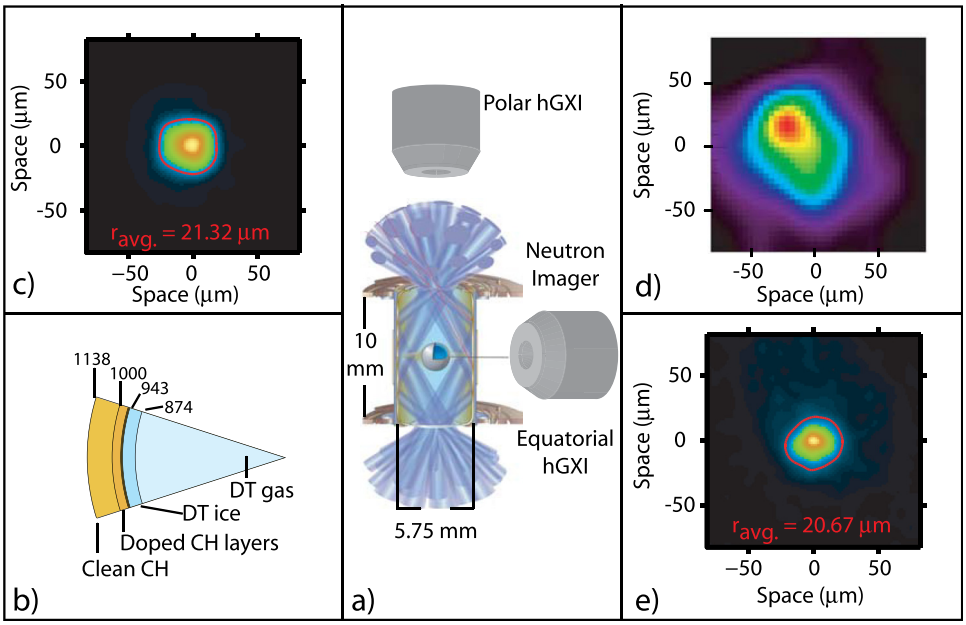

FIG. 1. Shot N120412 experimental setup, capsule composition, core x-ray, and neutron images. (a) Experimental setup, a 10 mm long, 5.75 mm diameter hohlraum, is irradiated using 192 laser beams with a combined energy of 1.66 MJ. The resulting hohlraum x-ray flux implodes a cryogenic capsule target, located in the center of the hohlraum. The x-ray self emission from the imploding capsule is imaged along the polar and equatorial axis using two harden hGXI diagnostics. Primary neutrons (14 MeV) created in the hot central core are down-scattered in the surrounding dense DT shell. The NI diagnostic images both the primary and down-scattered (6–10 MeV) neutrons along the equatorial axis. (b) A pie diagram representing the composition and initial dimensions, given in microns, of the spherical fusion capsule target. (c) An image of the x-ray self emission at peak compression as seen from the polar hGXI diagnostic. The red contour indicates an average radius of 21.32 μm at a value of 17% of peak emission. (d) The image of the down-scattered neutrons. The average radius, taken at the 17% contour of peak emission, was found to be 41 μm, and is indicative of the radius of the dense shell of DT ice that surrounds the core of the implosion. (e) An image of the x-ray emission at peak compression as seen from the equatorial hGXI diagnostic. The red contour indicates an average radius of 21.67 μm at a value of 17% of peak emission.

gain along each strip of the MCP varies with time, creating a total temporal length along each strip of ~230 to ~180 ps for the polar and equatorial hGXI, respectively. Additionally, the gain of each strip is typically delayed 200 ps from adjacent strips. Thus, images created by the pinhole array at different spatial locations are captured at different times, and a continuous record of the x-ray emission is recorded. Each hGXI has a magnification of 12×, a spatial resolution of ~10 μm, and is filtered with 2575 μm of Kapton ($C_{22}H_{10}N_2O_5$). The polar and equatorial hGXI have a temporal gain width of 100 ps and 40 ps, respectively. The quantum gain (electrons produced per incident photon) of the hGXI detector is expected to decrease approximately linearly by ~40% between 6 and 13 keV.

Figures 1(c) and 1(e) show the x-ray image of the hot core at peak x-ray emission taken along the polar and equatorial axes for an implosion experiment that used 1.66 MJ of total laser energy (shot N120412). The radius of emission is defined as the average radius of a contour taken at 17% of the maximum emission value. The red contour in Figs. 1(c) and 1(e) shows this 17% contour and indicates an average radius of ~21 μm along the polar and equatorial axes. The burn width of the implosion is defined as the full width half maximum (FWHM) of the integrated signal within the 17% contour of emission vs. time, and for this experiment was found to be 149 ± 50 ps. Surrounding the hot spot is the dense compressed shell of DT fuel and unablated plastic. Radiation hydrodynamic simulations indicate that the dense shell is at a much lower temperature than the hot spot. Consequently, the hGXI diagnostics only observe emission from the lower density hot core while emission from the colder dense shell is not detected. Simulations indicate that the 17% contour of the hot spot emission provides information on the inner radial shape of the cold dense DT fuel shell.

The diameter and density of the dense shell surrounding the hot spot are diagnosed by multiple neutron detectors that can discriminate between primary and down-scattered neutrons. At peak compression, deuterium and tritium ions fuse within the hot core, creating a so-called primary neutron, at an energy of 14.1 MeV, and a α particle at an energy of 3.5 MeV. Neutrons, which lose energy through inelastic collisions with atoms while propagating outwards through the dense shell of compressed DT fuel and unablated plastic, are referred to as down-scattered neutrons. The primary and down-scattered neturons are detected by the neutron imager (NI) diagnostic and neutron time of flight detectors (NTOF). Figure 1(d) is an image of the down-scattered neutrons with energies between 6 and 10 MeV, and shows the shape of the dense shell that surrounds the hot spot. The 17% contour of the down-scattered image has an average radius of 41 μm and is indicative of the outer radius of the dense shell. The density within this shell is found from ratio of the number of down-scattered neutrons to the number primary neutrons detected on the magnetic recoil spectrometer detector; for the experiment shown in Fig. 1, the density was found to be ~900 g/cc. The ion temperature of the hot core at stagnation is measured from the width in energy of the primary neutron spectrum and was found to be 1.84 keV for this experiment. Using the neutron yield, ion temperature, volume of the hot core, and the burn duration, the core pressure is inferred.[4]

For this experiment, the pressure of the compressed core at stagnation was found to be ~150 Gbar.

A physical picture of the origin and dynamics of the shock that is observed after the implosion has reached stagnation is developed using results from 1-D hydrodynamic simulations, which include radiation transport. The pressure within the hot core reaches a maximum as the inward material velocity of the core and the surrounding dense shell decelerates and approaches zero. At this time, the pressure within the central region of the hot core is approximately constant and the pressure begins to decrease rapidly beginning at a radius close to the inner edge of the dense shell. Surrounding the stagnated hot core and dense shell is a plasma comprised of ablator material. This surrounding plasma is at a much lower pressure than the peak stagnation pressure and has a material velocity that is still converging inwards at ~200 km/s. Simulations show a large, $\geq 10\times$ step in pressure, density, and material velocity, over a few microns in radius, at the interface between the outer edge of the dense shell and the surrounding plasma and indicates the shock front location at stagnation. After stagnation, this shock front location begins to propagate outwards in the laboratory frame, ahead of the expanding compressed core and shell material. As the shock moves outwards, the pressure of the core and shell material decreases and develops a parabolic profile with radius. As this occurs, the material velocity develops a linear dependence with radius, increasing from zero to a maximum value at the contact front located at the interface of the expanding material and shocked material. Across the contact front, the velocity of the expanding material is equal to the post-shock material velocity. Simulations indicate that these profiles develop as the shock front reaches a radius of ~150 μm approximately 200 ps after stagnation. In the laboratory frame, the velocity of the outward propagating shock can be related to the average energy density, or average pressure of the hot core and surrounding dense shell reached at stagnation.

The velocity of the shock can be related to the downstream material velocity via the Rankine-Hugoniot (RH) relations as

$$D = \frac{\left(u_2 - \frac{\rho_1}{\rho_2}u_1\right)}{\left(1 - \frac{\rho_1}{\rho_2}\right)}, \quad (1)$$

where, ρ, $u_{1,2}$, and D are the material density, material velocities, and shock velocity in the laboratory frame, respectively. Subscripts 1 and 2 denote the properties upstream and downstream of the shock front. For $u_2 \gg \rho_1 u_1/\rho_2$, Eq. (1) indicates that $D \propto u_2$, where u_2 is equal to velocity of the expanding material. To estimate the velocity of the expanding material, a self-similar solution that describes the expansion of a ball of gas into vacuum, with similar pressure and velocity profiles as those that develop during the expansion of the compressed core and dense shell, can be used.[18] This solution indicates that the velocity of the expanding material, u_2, will approach a value proportional to $\sqrt{2E/M}$ as the radius of expansion becomes much larger than the initial radius. Here, E represents the energy contained within the implosion, including both that of the hot core and shell material and M is the mass of this material. This simplified physical picture is used to show that expansion velocity of the contact front, and thus the shock velocity is proportional to the amount of energy contained within the implosion. The deposited energy can be related to the average of the pressure of the hot core and dense shell at stagnation.

As the shock expands, it sweeps up, compresses, and heats the surrounding material. Bremsstrahlung radiation is emitted from the shocked material. This radiation has been spatially and temporally resolved by the hGXI diagnostics, and is used to determine the shock front location and shock velocity. The shock velocity is related to the post-shock material temperature via the RH relations. It can be shown that $T_2 \propto (D - u_1)^2$, where T_2 is the downstream post-shock material temperature. As the shock velocity increases, the post-shock temperature, and thus radiative energy flux, F, that scales as $F \propto T_2^4$, increases rapidly. If the magnitude of the radiative energy flux is such that it modifies the shock dynamics as described by the RH relations, then the shock can be called a radiative shock. The observed laboratory frame shock velocity, taken together with mass density and temperature of the in-falling ablator plasma (inferred from analytic estimates), as well as the observed post-shock structure, indicates that the shock produced in these experiments can be described as a radiative shock.

III. RESULTS

A. Cryogenic implosion results

Figure 2 shows the temporal evolution of the x-ray emission detected by the polar hGXI diagnostic for shot N120412. Peak x-ray emission from the central core occurs on the first strip of the detector at $t = 0$. On the second strip of the detector, a ring of x-ray emission suddenly appears at t ≈ 200 ps and at an initial radius of 105 μm. The outgoing

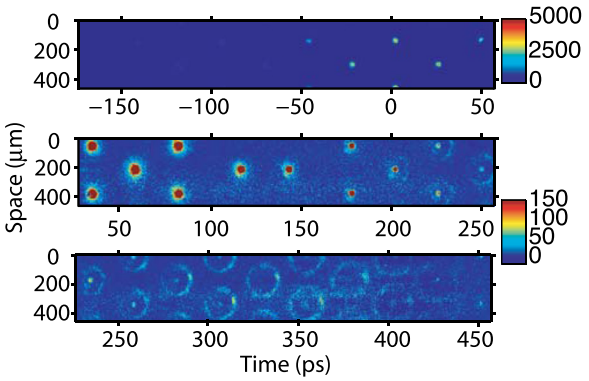

FIG. 2. Image from the polar hGXI diagnostic showing the spatial and temporal evolution of the x-ray emission along three strips for shot N120412. Time t = 0 denotes peak x-ray emission. Approximately 200 ps after peak x-ray emission, a limb-brightened shell of x-ray emission, created by a spherically expanding shock wave, suddenly appears at a radius of ~100 μm. This emission is observed to expand outwards until ~500 ps after peak x-ray emission, at which time the signal drops below the detectable level. The color scale has been changed between strip 1 and strips 2 and 3 to enhance the visibility of the shocked material.

spherical shock wave compresses and heats a shell of material. Radiation from this shock shell is limb-brightened and is detected as a ring of emission. This emission is then observed to expand outwards at a velocity of ~300 km/s, in the laboratory frame, over the next 300 ps before the luminosity drops below the detectable level of the instrument.

Insight into the cause of the sudden increase in the intensity of emitted radiation can be gained by considering the emission from the shocked material at a frequency ν and radial location r_o. This can be described by $I(r) = I_o e^{-\kappa_\nu \rho_o r}$, where $I(r)$ is the intensity of the emission, I_o and ρ_o are the intensity of emission and density at a location r_o within the plasma, κ_ν is the opacity at frequency ν, and r is the distance at which the light travels through the plasma at these conditions. The relatively sudden appearance of this ring of emission at a radius of ~100 μm, over a duration of ~50 ps, suggests a rapid increase in I_o, or a decrease in ρ_o, κ_ν, or a combination of all of these effects. All of these effects can occur for a shock wave that experiences a sudden decrease in upstream material density in conjunction with a sudden increase in upstream material temperature. Physically, this can occur at the location of the so-called ablation front, defined as the radius at which the ablator plasma becomes opaque to the x-ray flux of the hohlraum. Simulations, which will be discussed in more detail in Sec. V, show a rapid increase in spectral intensity at a radius of ~100 μm, as the shock front propagates into the ablation front, approximately 200 ps after the peak compression of the implosion has been reached.

Figure 3 shows data from two implosion experiments detailing the temporal evolution of the radius of x-ray emission produced by the expansion of the spherical shock wave after stagnation. The shock velocity in the laboratory frame is found to be ~300 km/s and is consistent with the velocity observed in a 1-D radiation hydrodynamic simulation. In Fig. 3, the square data points represent the radius of x-ray emission from the previously described implosion experiment, shot N120412. The triangular data points are the measured radii of the ring of x-ray emission vs. time observed on shot N110620. This shot used 1.42 MJ of laser energy to create the x-ray flux that compressed a fusion capsule target that was of similar dimensions and composition as shown in Fig. 1(b). The velocity of the shock is found by measuring the temporal rate of change of the limb radius, measured at the outward edge of the emission. This is done in order to minimize the uncertainties in the radial location due to the finite temporal resolution of the framing camera and from the limb-brightening of the shell of emission. The dashed lines in Fig. 3 represent the best linear fit to the expansion of the shock and indicate a shock velocity of 305 ± 47 km/s and 280 ± 69 km/s for the 1.66 and 1.42 MJ implosion experiment, respectively. The solid line is the radius of emission predicted by the radiation hydrodynamic code HYDRA.[19] Here, the simulated results are from a 1-D calculation of an implosion conducted with 1.6 MJ of laser energy and which reached a core stagnation pressure of ~150 Gbar. The simulated emission expands outwards at a velocity of 350 km/s, which is within the 1 σ error bar of the measured expansion velocity in the 1.66 MJ implosion experiment. The emission produced by the outgoing shock is observed up until ~500 ps after peak x-ray emission. At this time, the emission from the shock drops below the detectable level of the instrument. As no appreciable decrease in shock velocity is seen, the observed decrease in luminosity from the shock-heated matter is not due to the dissipation of the shock. As will be discussed in Sec. VI, simulations indicate that the reduction in luminosity in time results from a decline in the post-shock temperature and density that follows from changes in the upstream material properties.

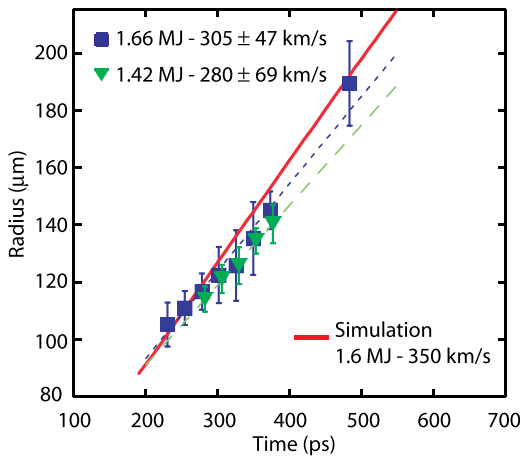

FIG. 3. The radius of x-ray emission produced by the outward going spherical shock wave vs. time. Data produced from a DT capsule implosion conducted with 1.66 MJ (squares) and 1.42 MJ (triangles) of laser energy is shown. The two dashed lines represent the results from a linear fit to the expansion data. The solid line represents the predicted radius of x-ray emission vs. time from a 1-D HYDRA simulation that used 1.6 MJ of laser energy to irradiate the hohlraum.

Figure 2 shows that the spatial width of the ring x-ray emission remains approximately constant with time and indicates emission from a shell shock-heated matter that has a width of ≤ 10 μm. This is consistent with the emission produced from the narrow cooling layer that exists in radiative shocks.[20] The width (FWHM) across the limb of x-ray emission is ~30–35 μm and has been spatially broadened by the finite temporal response of the detector. The measurements were made using the polar hGXI diagnostic, which has a temporal gain width of ~100 ps. For a shock velocity of ~300 km/s and a temporal resolution of 100 ps, the ~30–35 μm limb width indicates a thin region of emitting matter that is equal to or less than the resolution of the diagnostic of ~10 μm. As discussed in more detail in Secs. V and VI, in these experiments, radiation from a thin cooling layer which immediately follows the shock front is expected to be the largest contributor to the detected signal.

B. Convergent ablation results

X-ray emission created from the outgoing shock was also observed in the convergent ablation (ConA) experiment[21,22] N120409, which used the same laser pulse shape and nearly the same laser energy as the previously discussed 1.66 MJ DT capsule implosion. The expansion velocity of the

x-ray emission was measured to be 346 ± 7 km/s, consistent with the measured expansion velocity in the DT capsule implosion. Figure 4 shows the ConA experimental setup, the measured time resolved radiograph of the capsule implosion and subsequent x-ray emission imaged in one dimension, and a comparison of the measured and simulated radial location for the peak intensity of the expanding x-ray emission. In this ConA experiment, the x-ray flux was produced by 1.62 MJ of laser energy, which is similar to the 1.66 MJ of laser energy used to conduct the DT implosion N120412. In addition, the ConA experiment used 48.6 kJ of laser energy to create a Zn He-α x-ray probe to radiograph the capsule during the implosion. The dimensions and composition of the symmetry capsule target (Symcap) that were used are also shown in Fig. 4(a). The Symcap target is nominally the same as the DT layered target, except the DT ice layer has been replaced with an equivalent amount of CH mass and the DT gas fill is replaced with a higher pressure D_2^3He fill that reduces the convergence and neutron yield of the implosion. The capsule radiograph was imaged in one dimension by a 17 μm wide slit onto the DISC streak camera.[23] The resulting temporal resolution for this slit width was ~50 ps. An image of the measured radiograph that has been spatially and temporally averaged over 5 μm and 22.5 ps, respectively, is shown in Fig. 4(b). The DISC detector has been filtered with 375 μm of Kapton and 15 μm of zinc. The compressed CH shell creates the two dark limbs that converge inwards with time. Along the center of the spatial axis, a wire fiducial attenuates the x-ray probe and partially obscures the x-ray self emission from the compressed core at times ±500 ps from peak x-ray emission. At t ≈ 150 ps, two limbs of x-ray emission, created from the outward going shock, are observed to emerge and propagate outwards. The observation of two distinct limbs of x-ray emission is consistent with the 1-D imaging of a shell of expanding x-ray emission.

Figure 4(c) shows the measured average radius of the emission vs. time and shows that the shock expands at a nearly constant velocity over the duration of observation. The average radius of the x-ray emission was measured dividing the distance between the maximum intensity of the two limbs by two. Each data point is the average radius over the 22.5 ps time interval, with the error bars corresponding to the root mean squared deviation from the average radius over the time interval. Additionally, hydrodynamic simulations, in which forward Abel transformations are performed and convolved with the instrument response functions to generate simulated DISC radiographs, also predict the x-ray emission generated by the outward going shock after stagnation.[24] The simulated peak x-ray emission radius vs. time is also shown in Fig. 4(c) as the solid line, and is in good agreement with the measurement. The width and intensity of the limb of x-ray emission are determined by the limb-brightening of the shell of x-ray emission and by the finite temporal response of the detector. To determine the velocity of the shock, the average temporal rate of change of the radial location at the outward edge (FWHM) of the x-ray limb was measured and found to be 346 ± 7 km/s, which is consistent with the measured expansion velocity of 305 ± 47 km/s from the companion DT implosion.

IV. RADIATIVE SHOCKS

A radiative shock can be defined as a shock in which either the radiative pressure or radiative energy flux alters the shock dynamics.[25–27] In these experiments, it can be shown that the shock is expected to become radiative as it transitions into the lower density ablated plasma that has been heated to ~300 eV by the hohlraum x-ray flux. Here, the observed shock is determined to exist in a regime in which the radiative pressure is negligible compared to the material pressure, but where the radiative energy flux is comparable

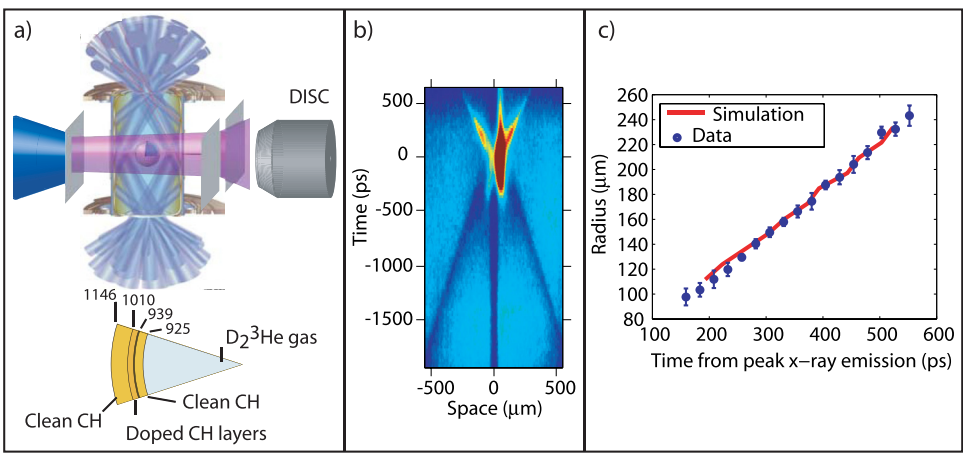

FIG. 4. (a) Details of the convergent ablation experimental setup and results from shot N120409. Here, a probe laser irradiates a zinc foil, creating a burst of x-rays that radiographs the capsule implosion over a duration of ~2 ns. A slit images the capsule radiograph in one direction onto the DISC streak camera, which temporally resolves the implosion. The dimensions in microns and composition of the capsule target are also shown. Here, a symmetry capsule target is used, which replaces the DT fuel layer and gas fill by an equivalent mass of CH and a D_2^3He gas fill, respectively. (b) The measured 1-D radiograph vs. time of a capsule implosion. The dense shell absorbs the x-ray probe creating two dark limbs, which converge inwards with time as the shell is compressed by the hohlraum x-ray flux. The dark absorption band located approximately at the center of the capsule is created by a wire fiducial and partially obscures the bright self emission from the core. Time t = 0 denotes the time of maximum self emission from the capsule core. Emission created by the outward going radiative shock is seen to appear at $t = \sim 150$ ps. (c) Radial location of the peak of emission from the outward going shock vs. time. Data shown in blue are in good agreement with the simulated emission location calculated with HYDRA shown in red.

to the in-flowing material energy flux. The structure of a radiative shock in this so-called radiative flux regime can be analytically described using a three-layer model.[20,25] The three different layers of the system are the region upstream of the shock front, the cooling layer, which exists immediately after the shock front, and the final downstream region, where the density, temperature, and pressure reach their final post-shock values. In the cooling layer of a radiative shock, the temperature initially rises sharply as the shock compresses and heats the in-flowing material; the layer then rapidly cools via radiation until it reaches the final down stream temperature. For systems in which the upstream material is optically thin to thermal radiation, the material density continues to rise from the initial shocked value through the cooling layer and reaches the final post-shock density at the back of the cooling layer. The radiative energy flux of such shocks can modify the shock front structure and create a final downstream state that can be quite different compared to shocks in which the radiative energy flux is negligible.

Qualitatively, the magnitude of the radiative flux required to impact the shock structure can be estimated by examining the Rankine-Hugoniot relationship for energy conservation including the radiative energy flux. In the frame of the shock, this is given by

$$\rho_2 U_2\left(e_2+\frac{1}{2}U_2^2+\frac{P_2}{\rho_2}\right)+F_2=\rho_1 U_1\left(e_1+\frac{1}{2}U_1^2+\frac{P_1}{\rho_1}\right)-F_1. \tag{2}$$

Here, ρ, P, e, and F are the material density, pressure, internal energy, and radiative energy flux, respectively, where γ is the adiabatic index and the subscripts 1 and 2 denote the initial upstream and final downstream quantities, respectively. In the shock frame, material flows into and out of the shock front at a velocity $U_1 = D - u_1$ and $U_2 = D - u_2$, where D, u_1, and u_2 are the shock velocity, upstream and downstream material velocities in the laboratory frame, respectively. Following the description for systems that are optically thick downstream and optically thin upstream, Eq. (2) can be rewritten as

$$\rho_2 U_2\left(e_2+\frac{1}{2}U_2^2+\frac{P_2}{\rho_2}\right)=\frac{\rho_1 U_1^3}{2}-F_1, \tag{3}$$

where radiative flux in the downstream region $F_2 = 0$, and $P_2 \gg P_1$ has been assumed. The right hand side of Eq. (3) depends only on the in-flowing material energy flux, given by $\rho_1 U_1^3/2$ and the radiative energy flux that propagates out from the edge of the cooling layer upstream. For systems with an upstream region in which the optical depth for the thermal radiation is small, as is expected for the upstream plasma in this experiment, the radiative flux that leaves the leading edge of the cooling layer and enters into the upstream region can be approximated[20] as $F_1 \approx 2\sigma T_2^4$. Here, σ is the Stefan-Boltzmann constant. For such systems, when $\rho_1 U_1^3/4\sigma T_2^4 \lesssim 1$, the effect of the radiative energy flux on the dynamics of the shock structure and final post-shock state must be considered. An important caveat to this description is that it only strictly describes shocks that have reached a steady profile.

To qualitatively show that the shock created in these experiments is expected to produce a radiative flux large enough to impact the shock structure, the ratio of material to radiative energy flux will be approximated using information from observations and from basic physical arguments that are used to estimate the material conditions upstream and downstream of the shock front. As previously discussed in Sec. II, observations indicate that emission from shock-heated matter appears suddenly and is consistent with a shock that experiences a sudden decrease/increase in upstream material density/temperature. This relatively sudden change in density and temperature can occur at the so-called ablation front, defined here as the radius at which the ablator material becomes opaque to the x-ray flux of the hohlraum. Upstream of the ablation front (towards larger radii), the ablator material is heated to $\sim$250 eV and is in thermal equilibrium with the hohlraum radiation flux. Downstream from the ablation front (towards smaller radii), the material has been compressed, but remains cooler as it does not directly absorb x-ray radiation from the hohlraum. To estimate the material energy flux at the shock front as the shock propagates past the ablation front, the in-flowing material velocity in the frame of the shock, U_1, and density at the ablation front need to be estimated. The radiative energy flux at the ablation front can also be approximated by estimating the post-shock material temperature, which like the material energy flux, is also strongly dependent on U_1. It is found that U_1 at this location is significantly larger than the shock velocity D observed in the laboratory frame, due to the comparable upstream in-flowing material velocity u_1.

The in-flowing material velocity at the ablation front is estimated using the following physical picture. As the capsule implodes, the x-ray flux continuously ablates material from the CH shell. The ablated material is removed with an outward velocity equal to the isothermal ion sound speed in a partial ionized CH plasma, $c_s = \sqrt{(Z_{avg}+1)KT_{rad}/M_{avg}} \approx 115\,\mathrm{km/s}$, for $Z_{avg}=2.5, KT_{rad}=250\mathrm{eV}$, and $M_{avg}\approx 6.5 m_p$, where m_p is the proton mass. In the laboratory frame, the in-flowing material velocity is given by, $u_1 = c_s - v_{imp}$, where v_{imp} is the implosion velocity of the CH shell. The previously discussed ConA experiment, which used nearly the same laser conditions, measured the peak implosion velocity of the fuel to be 300km/s, setting the upper limit of $u_1 = -185\mathrm{km/s}$ in this experiment. With an observed shock velocity of $\sim$300km/s, an upper limit of $U_1 = 485\mathrm{km/s}$ can be used when calculating the in-flowing material energy flux and when estimating the post-shock temperature. The in-flowing material energy flux also depends on the upstream density, ρ_1. At the ablation front, the upstream density can be estimated to be $\sim$1 g/cc using the relation $\sigma T_{rad}^4 = 4\rho_1 c_s^3$, which describes the balance of energy flux from an ablative heat wave.[28] With $U_1 = 485\mathrm{km/s}$ and $\rho_1 = 1\,\mathrm{g/cc}$, the in-flowing material energy flux is found to be 5.7 x 10^{19} W/m^2.

The radiative flux, F_1, can be estimated by solving for the post-shock temperature, T_2. The immediate post-shock temperature, T_{ds} and the final material temperature after the

cooling layer, T_2, both increase due to the upstream material velocity, u_1, being comparable to the shock velocity D, and due to the fact that the upstream material temperature has been heated to ~250 eV. Qualitatively, this effect can be seen by estimating the immediate downstream temperature, T_{ds}, using the RH relations in the limit of $P_2 \gg P_1$, and neglecting the radiative flux,

$$T_{ds} \approx 2\frac{A}{k_b(Z+1)}\frac{\gamma_2 - 1}{(\gamma_2+1)^2}(D-u_1)^2 + T_1. \quad (4)$$

Here, k_b is the Boltzmann constant, A is average atomic weight, and Z is the average ionization state. As previously discussed, in this experiment, the hohlraum x-ray flux heats the ablated upstream in-flowing material to a $T_1 \approx 250$ eV. Equation (4) indicates that both the large upstream material velocity, u_1, and temperature, T_1, will significantly increase the post-shock temperature compared to a system in which both u_1 and T_1 are negligible. The radiative flux, assuming that the cooling layer is optically thin, can be approximated as, $F_1 \approx 2\sigma T_2^4$. Using the analytic relationships given by McClarren *et al.*, the final downstream temperature, T_2, was estimated using an normalized upstream initial pressure $p_{on} = (Z_{avg}+1)k_bT_1/(M_{avg}U_1^2)$. Here, T_1 was taken to be 250 eV, equal to the effective hohlraum radiation temperature after stagnation. Using a post-shock $Z_{avg} = 3.5$, $\gamma_2 = 4/3$, a shock velocity $D = 300$ km/s, and $u_1 = -185$ km/s, a post-shock temperature $T_2 = 374$ eV and subsequent radiative flux $F_1 = 4\times10^{19}$ W/m^2 are estimated. The ratio of material to radiative energy flux in this experiment is then expected to be $\rho_1 U_1^3/2F_1 \approx 1$, which indicates that the radiative flux created by the shock produced in these experiments is expected to modify the shock dynamics. This estimate does not take into account the effect of the upstream radiative precursor, which will raise the upstream material temperature and pressure. Additionally, this estimate assumes that radiative flux from the downstream region can be modeled as a Planckian source. To more accurately model the properties of the shock in these experiments, hydrodynamic simulations, that include radiation transport, were performed.

V. SIMULATION

A finely zoned radiation hydrodynamic simulation of a capsule implosion in 1-D details the shock evolution and shows a rapid rise in the radiance of the shock-heated matter that is consistent with experimental observations. The radiative hydrodynamic simulations are done in one-dimensional (spherical) geometry using the HYDRA code in Lagrangian mode. A frequency-dependent radiation source, derived from a fully integrated 2-D hohlraum simulation, is imposed as a boundary condition at the exterior of a helium channel surrounding the plastic shell of the capsule. Three temperatures (electron, ion, and radiative) are evolved under the assumption of local thermodynamic equilibrium. The equations for the multi-group radiation transport (using a total of 60 groups: 25 below 1 keV, 25 between 1 and 5 keV, and 10 up to 100 keV) are solved in the diffusive limit, as is the thermal electron conduction, where a flux limiter of 0.05 is used. The equations of state are similar to QEOS, with a Thomas-Fermi model for ionization and opacities. The capsule is more finely meshed than is usual for implosion calculation in order to conserve a resolution better than 0.25 μm in the cooling layer of the expanding shock under inquiry. To check that the diffusive radiation treatment was not flux-limited, the one-dimensional problem was also solved using a discrete ordinate (S_N) method. The outgoing shock characteristics (temperature, velocity, precursor, and cooling layer) were found to be very similar in both simulations. The simulated x-ray radiance at the detector was calculated by integrating the radiation transport equation, $dI/ds = J - \kappa I$ along ray paths from each mesh location to the detector plane. Here, I is the specific intensity, s is the distance along the ray, J is the specific emissivity, and κ is the opacity. The rays pass through a pinhole 10 μm in diameter placed 100 mm from the implosion, creating an image at the detector plane. The radiance of the image is found by using the local emissivity from each mesh location and then by calculating the opacity through the plasma along the path of the ray to the detector for multiple groups of radiation energies. The emissivity and opacity are held constant, equal to the zone centered value, across each zone of the mesh. The calculated radiance includes the attenuation of the radiation by the diagnostic filtering.

Figure 5 presents results from a simulation in which 1.6 MJ of laser energy is used to irradiate the hohlraum wall, and a core stagnation pressure of 150 Gbar was reached. These parameters are similar to the laser energy and the inferred stagnation pressure for the experiment discussed above. Figures 5(a)–5(c) show the evolution of the electron temperature, material density, and velocity at times $\Delta t = 0$, 100, and 200 ps from stagnation, respectively. Figure 5(d) shows the predicted radiance, taking into account the detector filtering, at these time intervals. From these simulations, it is observed that the outward going shock is located at the outer edge of the dense shell of DT fuel and unablated CH at $\Delta t = 0$. Figure 5(a) shows this initial state. Here, the density profile shows a shell with a peak density of 359 g/cc at a radius of 60 μm. This shell surrounds the lower density central core which at this time has a peak electron temperature of 1.75 keV. The dashed line is the material velocity and indicates that the implosion has reached stagnation as the velocity of the core and dense shell is nearly zero. At radii larger than the radius of the dense shell, a decreasing gradient in the density profile has developed. This unablated material is still flowing inwards at a velocity of ~200–250 km/s. At this time, the electron temperature at r = 150 μm is equal to the hohlraum radiation temperature of 260 eV, and the temperature profile indicates the ablation front is at a radius of ~120 μm. The temperature within the low pressure unablated density gradient is ~50 eV.

Figure 5(b), at $\Delta t = 100$ ps from stagnation, shows the shock now propagating outwards into the surrounding CH ablator. The sharp discontinuity in the electron temperature, density, and material velocity at r = ~80 μm, with a positive post-shock velocity, indicates the shock front location. At $\Delta t = 100$ ps from stagnation, Fig. 5(d) shows that the radiance has decreased at all radii from the radiance that was

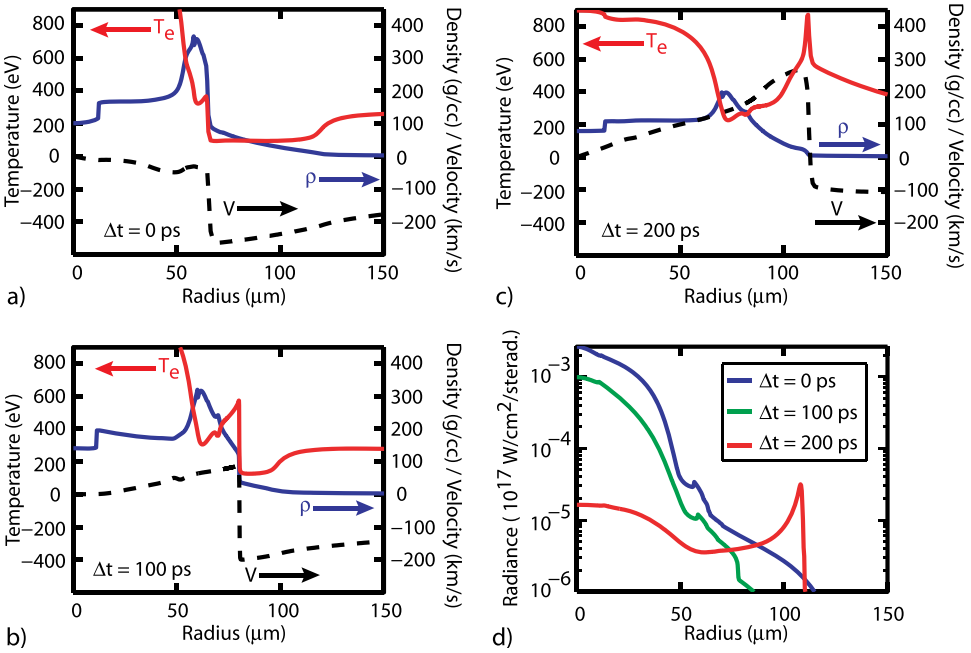

FIG. 5. Results from a 1-D radiation hydrodynamic simulation showing the evolution of the electron temperature (red), material density (blue), and material velocity (dashed black) profiles at $\Delta t = 0$, 100, and 200 ps from stagnation, in (a), (b), and (c), respectively. A strong shock is located at the interface between the dense shell of DT fuel and unablated CH plasma. After stagnation, the shock propagates outwards into the lower density surrounding CH plasma. (d) The simulated radiance of the material, including the detector filter transmission, at $\Delta t = 0$, 100, and 200 ps from stagnation. Simulations are in agreement with experimental observations that show the sudden appearance of a ring of x-ray emission at a radius of $\sim 100\,\mu$m hundreds of picoseconds after peak x-ray emission.

emitted at stagnation. This is qualitatively consistent with the decrease in radiance 100 to 200 ps after peak x-ray emission that was observed in the experiment and can be seen in Fig. 2. The location at which the in-flowing plasma becomes opaque to the hohlraum x-ray flux, the so-called ablation front, is located at $r \approx 100\,\mu$m in Fig. 5(b) and can be found by observing the relatively rapid change in the material temperature.

In Fig. 5(c), the shock has propagated past the so-called ablation front and into a lower density region of CH plasma, where the material has been heated to 250 eV by the x-ray flux from the hohlraum. Both the decrease in upstream density and the increase in the immediate post-shock temperature result in a sudden increase in the radiance that is observed at a radius corresponding to the shock front location at $r = 108\,\mu$m. This sudden increase in radiance, approximately 200 ps after stagnation, can clearly be seen in Fig. 5(d) and leads to a limb-brightened ring of detected emission, consistent with observations from multiple implosion experiments.

As seen in Fig. 5(c), the existence of a radiative precursor, as well as the narrow spike in temperature at the shock front, followed by a rapid cooling in material temperature, indicates that radiation transport from the shock-heated matter is significantly modifying the shock front structure. The sharp, so-called Zel'dovich spike in temperature located just behind the shock front, as well as observation that the upstream and downstream electron temperatures are nearly equal, indicates the formation of a so-called super critical shock. In such systems, the radiation temperature is out of equilibrium with the material temperature in the cooling layer just behind the shock front.[18] As will be discussed in Sec. VI, in these experiments, the diagnostic is filtered such that the measurement detects emission at x-ray energies that are several times the predicted immediate post-shock temperature. Therefore, the spectral intensity that is detected is expected to be highly sensitive the temperature of the radiating material. Due to this, radiation from the narrow shell of material that immediately follows the shock front and which simulations suggest has been heated to a temperature that exceeds the upstream and downstream material by 300 eV is expected to dominate the x-ray emission at a radius of $\sim 100\,\mu$m, 200–300 ps after peak compression. This is consistent with the observed narrow source size of the observed x-ray emission.

VI. LUMINOSITY

The amplitude and temporal evolution of the x-ray luminosity emitted from the shock-heated matter have been measured and found to be in good agreement with results from radiation hydrodynamic simulations. The temporal evolution of the x-ray luminosity from a stellar supernova is often used to infer information about age and type of progenitor. Observations of such light curves show variations in luminosity with time, which have been attributed to variations in the density of the circumstellar medium.[29] The ability to create, diagnose, and simulate such x-ray light curves offers an opportunity to study x-ray emission from a system directly relevant to astrophysical radiative shocks. Additionally, the spatial variance in limb-brightened emission intensity can be used to study hydrodynamic instabilities that can develop during and after the implosion.

The solid squares and triangles in Fig. 6 show the temporal evolution of the luminosity that was measured for the two cryogenic DT implosion experiments previously discussed conducted with 1.66 and 1.42 MJ of laser energy, respectively. The solid curves represent the luminosity predicted from HYDRA simulations in which the radiated luminosity was convolved with the temporal instrument response and material filtering to generate predicted x-ray light curves. The upper and lower solid curves are the simulated luminosity expected that result from using 1.6 and 1.4 MJ of energy to irradiate the hohlraum, respectively. The range of

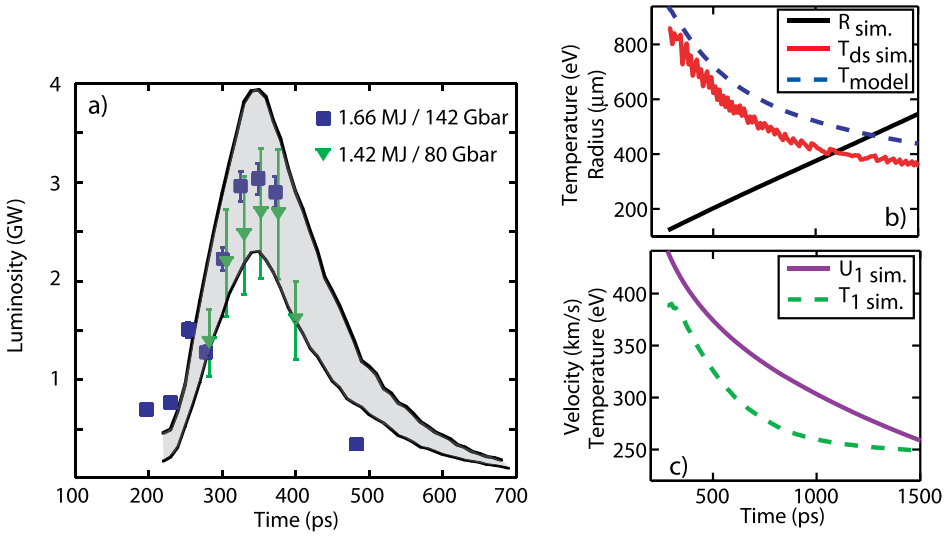

FIG. 6. (a) Luminosity of the limb-brightened ring of x-ray emission vs. time, at x-ray energies between 5.9 and 12.4 keV. The solid squares and triangles are the observed luminosity produced from an implosion conducted with 1.66 and 1.42 MJ of laser energy, respectively. The solid lines are the predicted luminosity profiles from 1-D hydrodynamic simulations. The upper curve is from a simulation that used 1.6 MJ of laser energy and the lower curve is from a simulation that used 1.4 MJ of laser energy, to irradiate the hohlraum, respectively. (b) Results from the 1.6 MJ simulation showing the temporal evolution of the shock front (black), the peak post-shock electron temperature (red), and a simple analytic prediction given by Eq. (4) of the immediate post-shock temperature (dashed). (c) The temporal evolution of the in-flowing material velocity, U1 (solid), and upstream temperature, T1 (dashed), taken from the simulation conducted with 1.6 MJ of laser energy.

x-ray energies detected is estimated by multiplying the thermal spectrum from the expected peak shock temperature of 800 eV with the spectral response of the 2.5 mm of Kapton filtering. It is found that the peak of the spectral transmission occurs at 8.2 keV and that the measurement is sensitive over a spectral range from 5.9 to 12.4 keV, where the spectral range has been defined to be the energy at which 10% of the peak transmission is reached. Due to the diagnostic filtering, the power radiated from the material located at the sharp spike in temperature immediately following the shock front dominates the signal that is detected. Simulations show that the emission from the material immediately following the shock front is non-Planckian. The observed and simulated maximum luminosity is within 50% of each other and the amplitude of both the measured data and the simulated results shows a similar temporal evolution. The temperature of the shock-heated matter is expected to be on the order of ~1 keV, and therefore the observed luminosity between 5.9 to 12.4 keV represents a small fraction of the total luminosity of the shock-heated matter. In the simulations, the peak luminosity above an x-ray energy of 1 keV was found to be 2.25 TW.

The luminosity of x-rays observed in these experiments is strongly dependent on the post-shock temperature. Here, bremsstrahlung or free-free emission generated from the forward going shock, is the primary source of x-rays. The luminosity over the observed spectral range scales as

$$L \propto Z^2 n_e n_i T_{ds}^{1/2} V \left[-e^{-\frac{E}{k_b T_{ds}}} \right] \Big|_{E_{min}}^{E_{max}}. \quad (5)$$

Here, Z is the ionization state, n_e is the electron density, n_i is the ion density, T_{ds} is the immediate post-shock electron temperature, V is the volume of narrow shell of shocked material that immediately follows the shock front, and E_{min} and E_{max} are the lower and upper spectral energy range of the measurement, respectively. The luminosity from Eq. (5) can be used to estimate the power of the non-Planckian shell of emission that immediately follows the shock front. However, unlike the detailed simulations, this estimate does not include the effect of the attenuation of the radiation by the surrounding plasma. Simulations indicate that the mean free path of radiation at this location, calculated using the Rosseland mean opacity, is ~250 μm. This mean free path is much larger than the thickness of the thin shell of radiating shock-heated matter that dominates the measurement. As seen in Fig. 6, simulations indicate that the luminosity from the shock-heated matter increases as the amount of laser energy used to irradiate the hohlraum is increased. For implosions with equivalent amounts of compressed mass, an increase in the amount of laser energy will increase the amount of energy deposited into the implosion and in turn increase the outward going shock velocity. This leads to an increase in the post-shock temperature, T_{ds}. Since our observation is centered at 8.2 keV, which is several times the expected shock temperature, a small change in the post-shock temperature will result in a relatively large change in the observed luminosity. For example, with 2500 μm of Kapton filtering, and at a fixed charge state, density, and volume, the peak spectral intensity is found to change by ~50% as the T_{ds} is changed by 10% from 1000 to 900 eV.

In both the measured and simulated x-ray light curves, the luminosity initially increases over the first ~100 ps of observation reaches a maximum value at ~350 ps from peak x-ray emission, and then rapidly decreases by ~5–7X over the next 150 ps. Post-processing the luminosity data from the simulations, it was found that the rapid increase in luminosity over the first 100 ps of observation is due to the 100 ps temporal gain width of the detector.

The rapid decline in luminosity within the observed spectral range is determined to be caused by a decrease in the shocked material density and post-shock temperature. As the measurement is made over a spectral range that is several times the temperature of the shocked material, the sharp decline in luminosity is mostly due to the decrease of the post-shock material temperature. One can estimate the decline in luminosity due solely to the decrease in material density by taking the ratio of Eq. (5) for two different radial locations and assuming a fixed charge state and temperature. This ratio of initial to final luminosity can then be written as $R = (n_{eo}/n_{ef})^2 V_i/V_f$, where the i and f subscripts denote the inital and final quantities, respectively. The simulated density profile is found to obey a $\rho \propto r^{-1.8}$ dependence. Data from the 1.66 MJ implosion experiment, shot N120412, indicate a luminosity ratio $R \approx 5-7$, as the radius of the shock expands 130 μm to 180 μm. The simulations indicate that the width of the shock changes only slightly with time; thus, taking the width as approximately constant, $V_i/V_f \approx r_i^2/r_f^2$, where r is the radius of the shock. With these conditions, the expected ratio of luminosity between 130 to 180 μm for a fixed post-shock temperature is $\sim$1.7, much less than the observed or simulated ratio. This estimate isolates the effect of decreasing density on the luminosity by assuming a fixed post-shock temperature. However, as shown in Fig. 6(b), the post-shock electron temperature is not constant, but rather is observed to decline with time.

Observations and simulations of the temporal evolution of the shock front radius, shown in Figs. 3 and 6(b), respectively, show that the shock velocity is approximately constant, indicating that the decline in post-shock temperature is not due to the deceleration of the shock. Examining Eq. (4), it is found that the post-shock temperature can decrease for a constant shock velocity D, if either the upstream material velocity, u_1, or upstream temperature, T_1, decrease. Figure 6(c) shows that the simulated in-flowing material velocity $U_1 = D - u_1$, and T_1 are both decreasing with time. As the shock propagates outwards in time to larger radii, the material density and optical depth both decrease. As the upstream material becomes optically thin to the radiation from the post-shock material, the temperature of the upstream precursor drops and approaches the radiation temperature of the hohlraum. Additionally, the decrease in U_1 with time is a result of the smaller u_1 at larger radii. At later times and larger radii, the ablated material which with the shock interacts was generated at earlier times in the capsule implosion, where the relative difference between $|c_s - V_{imp}|$ is smaller. Using the simulated values for U_1, and T_1, the post-shock temperature T_{ds} was estimated using Eq. (4) and is shown as the dashed curve in Fig. 6(b). The analytic estimate of T_{ds} slightly overestimates the simulated value, but has a very similar temporal dependence, indicating the important role played by the upstream temperature and in-flowing material velocity on the post-shock temperature and subsequently on the luminosity from the shock-heated matter. In simulations, the post-shock temperature is found to decrease from an initial temperature $T_i = 820$ eV at a radius of 130 μm to a final temperature $T_f = 695$ eV at a radius of 180 μm. To estimate the effect of the decline in temperature on the luminosity, the ratio of initial to final luminosity $(T_i^{1/2}/T_f^{1/2})(e^{-5.9/T_i} - e^{-12.4/T_i})/(e^{-5.9/T_f} - e^{-12.4/T_f})$ is taken and is found equal to $\sim$4, indicating a 4$\times$ decline in luminosity due to the decreasing temperature. This decline, taken together with the expected fall in luminosity of 1.6$\times$ from the decrease in density, predicts an overall reduction of 6.6$\times$ in luminosity from 130 to 180 μm, similar to the decrease observed in both the measurement and simulation.

VII. CONCLUSIONS

In conclusion, indirect drive inertially confined fusion implosion experiments at the National Ignition Facility have produced a spherically expanding radiative shock wave in the laboratory. One dimensional radiation hydrodynamic simulations show that a shock propagates outwards, ahead of the expansion of the dense shell of assembled fuel and ablator material after stagnation. Radiation from shock-heated matter is observed to appear suddenly at a radius of $\sim$100 μm, approximately $\sim$200 ps after peak x-ray emission. The expansion of the shock-heated matter indicates a shock velocity of $\sim$300 km/s in the laboratory frame. Simulations also show a rapid rise in the detected radiance at a radius of $\sim$100 μm, which coincides with the shock propagating down a density gradient past the so-called ablation front location into a plasma with a density of $\sim$1 g/cc, which is flowing inward at a velocity of $\sim$150 km/s and that has been heated to 250 eV by the x-ray flux of the hohlraum. Analytic estimates indicate that the velocity of the observed shock, taken together with the expected in-flowing material density, temperature, and velocity, creates a shell of shock-heated matter with a radiative energy flux that is of order of the in-flowing material energy flux, and therefore expected to modify the shock dynamics in these experiments. The simulation supports this estimate and predicts the formation of a radiative shock wave, with a radiative precursor upstream of the shock front, a sharp so-called Zel'dovich spike in temperature at the shock front, followed by a cooling layer where the temperature rapidly declines to a post-shock temperature that is approximately equal to the temperature of the upstream precursor. Additionally, the temporal evolution of the absolute x-ray luminosity between 5.9 and 12.4 keV from the shock-heated matter was measured and found to be in agreement with the luminosity predicted from radiation hydrodynamic simulations. Simulations indicate that the decline in luminosity follows a decrease in the post-shock temperature and density that occurs as the upstream material density, temperature, and in-flowing velocity all decrease as the shock propagates outwards in the laboratory frame. The magnitude of the decline was estimated by calculating the power radiated via bremsstrahlung emission using the simulated values for the temperature and density. This estimate was found to be consistent with observed and simulated luminosity decline.

In the future, by modifying the capsule composition and dimensions, as well as by changing the laser drive conditions, the shock velocity and radiative properties could be tailored to study various regimes related to supernova remnants. In these experiments, the absolute luminosity of x-ray emission from the forward and reserve shock waves can be

measured and used to test hypotheses to better understand the observed x-ray emission from supernovae.

ACKNOWLEDGMENTS

This work was performed under the auspices of the US DOE by LLNL under Contract DE-AC52-07NA27344 and supported by LDRD Grant 11-ER-050.

The work performed by G.G. has received funding from the European Research Council under the European Community's Seven Framework Program (FP7/2007-2013)/ ERC Grand Agreement No. 2568973.

[1]L. A. Lopez, E. Ramirez-Ruiz, D. Huppenkothen, C. Badens, and D. A. Pooley, ApJ **732**, 114 (2011).
[2]S. Park, D. N. Burrows, G. P. Garmire, J. A. Nousek, R. McCray, E. Michael, and S. Zhekov, ApJ **567**, 314 (2002).
[3]E. I. Moses and C. R. Wuest, Fusion Sci. Technol. **47**, 314 (2005).
[4]S. H. Glenzer, D. A. Callahan, A. J. MacKinnon, J. L. Kline, G. Grim, E. T. Alger, R. L. Berger, L. A. Bernstein, R. Betti, D. L. Bleuel, T. R. Boehly, D. K. Bradley, S. C. Burkhart, R. Burr, J. A. Caggiano, C. Castro, D. T. Casey, C. Choate, D. S. Clark, P. Celliers, C. J. Cerjan, G. W. Collins, E. L. Dewald, P. DiNicola, J. M. DiNicola, L. Divol, S. Dixit, T. Doppner, R. Dylla-Spears, E. Dzenitis, M. Eckart, G. Erbert, D. Farley, J. Fair, D. Fittinghoff, M. Frank, L. J. A. Frenje, S. Friedrich, D. T. Casey, M. G. Johnson, C. Gibson, E. Giraldez, V. Glebov, S. Glenn, N. Guler, S. W. Haan, B. J. Haid, B. A. Hammel, A. V. Hamza, C. A. Haynam, G. M. Heestand, M. Hermann, H. W. Hermann, D. G. Hicks, D. E. Hinkel, J. P. Holder, D. M. Holunda, J. B. Horner, W. W. Hsing, H. Huang, N. Izumi, M. Jackson, O. S. Jones, D. H. Kalantar, R. Kauffman, J. D. Kilkenny, R. K. Kirkwood, J. Klingmann, T. Kohut, J. P. Knauer, J. A. Koch, B. Kozioziemki, G. A. Kyrala, A. L. Kritcher, J. Kroll, K. L. Fortune, L. Lagin, O. L. Landen, D. W. Larson, D. LaTray, R. J. Leeper, S. L. Pape, J. D. Lindl, R. Lowe-Webb, T. Ma, J. McNaney, A. G. MacPhee, T. N. Malsbury, E. Mapoles, C. D. Marshall, N. B. Meezan, F. Merrill, P. Michel, J. D. Moody, A. S. Moore, M. Moran, K. A. Moreno, D. H. Munro, B. R. Nathan, A. Nikroo, R. E. Olson, C. D. Orth, A. E. Pak, P. K. Patel, T. Parham, R. Petrasso, J. E. Ralph, H. Rinderknecht, S. P. Regan, H. F. Robey, J. S. Ross, M. D. Rosen, R. Sacks, J. D. Salmonson, R. Saunders, J. Sater, C. Sangster, M. B. Schneider, F. H. Seguin, M. J. Shaw, B. K. Spears, P. T. Springer, W. Stoeffl, L. J. Suter, C. A. Thomas, R. Tommasini, R. P. J. Town, C. Walters, S. Weaver, S. V. Weber, P. J. Wegner, P. K. Whitman, K. Widmann, C. C. Widmayer, C. H. Wilde, D. C. Wilson, B. V. Wonterghem, B. J. MacGowan, L. J. Atherton, M. J. Edwards, and E. I. Moses, Phys. Plasmas **19**, 056318 (2012).
[5]John Sarrao, "Basic research directions for user science at the National Ignition Facility," NNSA and US DOE Office of Science (2011).
[6]B. A. Remington, R. P. Drake, and D. D. Ryutov, Rev. Mod. Phys. **78**, 755 (2006).
[7]J. C. Bozier, G. Thiell, J. P. L. Breton, S. Azra, M. Decroisette, and D. Schirmann, Phys. Rev. Lett. **57**(11), 1304 (1986).
[8]S. Bouquet, C. Stéhlé, M. Koenig, J.-P. Chièze, A. Benuzzi-Mounaix, D. Batani, S. Leygnac, X. Fleury, H. Merdji, C. Michaut, F. Thais, N. Grandjouan, T. Hall, E. Henry, V. Malka, and J.-P. J. Lafon, Phys. Rev. Lett. **92**, 225001 (2004).
[9]A. B. Reighard, R. P. Drake, K. K. Dannenberg, D. J. Kremer, M. Grosskopf, E. C. Harding, D. R. Leibrandt, S. G. Glendinning, T. S. Perry, B. A. Remington, J. Greenough, J. Knauer, T. Boehly, S. Bouquet, L. Boireau, M. Koenig, and T. Vinci, Phys. Plasmas **13**, 082901 (2006).
[10]A. J. Visco, R. P. Drake, S. H. Glenzer, T. Döppner, G. Gregori, D. H. Froula, and M. J. Grosskopf, Phys. Rev. Lett. **108**(14), 145001 (2012).
[11]K. Shigemori, T. Ditmire, B. A. Remington, V. Yanovsky, D. Ryutov, K. Estabrook, M. J. Edwards, A. J. MacKinnon, A. M. Rubenchik, K. A. Keilty, and E. Liang, ApJ **533**, L159 (2000).
[12]T. Ditmire, K. Shigemori, B. A. Remington, K. Estabrook, and R. A. Smith, ApJS **127**, 299 (2000).
[13]M. J. Edwards, A. J. MacKinnon, J. Zweiback, K. Shigemori, D. Ryutov, A. M. Rubenchik, K. A. Keilty, E. Liang, B. A. Remington, and T. Ditmire, Phys. Rev. Lett. **87**, 085004 (2001).
[14]J. Grun, J. Stamper, C. Manka, J. Resnic, R. Burris, and B. H. Ripin, Appl. Phys. Lett. **59**, 246 (1991).
[15]J. D. Lindl, P. Amendt, R. L. Berger, S. G. Glendinning, S. H. Glenzer, S. W. Haan, R. L. Kauffman, O. L. Landen, and L. J. Suter, Phys. Plasmas **11**, 339 (2004).
[16]S. W. Haan, J. D. Lindl, D. A. Callahan, D. S. Clark, J. D. Salmonson, B. A. Hammel, L. J. Atherton, R. C. Cook, M. J. Edwards, S. Glenzer, A. V. Hamza, S. P. Hatchett, M. C. Herrmann, D. E. Hinkel, D. D. Ho, H. Huang, O. S. Jones, J. Kline, G. Kyrala, O. L. Landen, B. J. MacGowan, M. M. Marinak, D. D. Meyerhofer, J. L. Milovich, K. A. Moreno, E. I. Moses, D. H. Munro, A. Nikroo, R. E. Olson, K. Peterson, S. M. Pollaine, J. E. Ralph, H. F. Robey, B. K. Spears, P. T. Springer, L. J. Suter, C. A. Thomas, R. P. Town, R. Vesey, S. V. Weber, H. L. Wilkens, and D. C. Wilson, Phys. Plasmas **18**, 051001 (2011).
[17]S. Glenn, J. Koch, D. K. Bradley, N. Izumi, P. Bell, J. Holder, G. Stone, R. Prasad, A. MacKinnon, P. Springer, O. L. Landen, and G. Kyrala, Rev. Sci. Instrum. **81**, 10E539 (2010).
[18]Y. B. Zel'dovich and Y. P. Raizer, *Physics of Shock Waves and High Temperature Hydrodynamic Phenomena* (Dover, Mineola, New York, 2002).
[19]M. M. Marinak, G. D. Kerbel, N. A. Gentile, O. Jones, D. Munro, S. Pollaine, T. R. Dittrich, and S. W. Haan, Phys. Plasmas **8**, 2275 (2001).
[20]R. G. McClarren, R. P. Drake, J. E. Morel, and J. P. Holloway, Phys. Plasmas **17**, 093301 (2010).
[21]D. G. Hicks, B. K. Spears, D. G. Braun, R. E. Olson, C. M. Sorce, P. M. Celliers, G. W. Collins, and O. L. Landen, Phys. Plasmas **17**, 102703 (2010).
[22]D. G. Hicks, N. B. Meezan, E. L. Dewald, A. J. Mackinnon, R. E. Olson, D. A. Callahan, T. Doppner, L. R. Benedetti, D. K. Bradley, P. M. Celliers, D. S. Clark, P. D. Nicola, S. N. Dixit, E. G. Dzenitis, J. E. Eggert, D. R. Farley, J. A. Frenje, S. M. Glenn, S. H. Glenzer, A. V. Hamza, R. F. Heeter, J. P. Holder, N. Izumi, D. H. Kalantar, S. F. Khan, J. L. Kline, J. J. Kroll, G. A. Kyrala, T. Ma, A. G. MacPhee, J. M. McNaney, J. D. Moody, M. J. Moran, B. R. Nathan, A. Nikroo, Y. P. Opachich, R. D. Petrasso, R. R. Prasad, J. E. Ralph, H. F. Robey, H. G. Rinderknecht, J. R. Rygg, J. D. Salmonson, M. B. Schneider, N. Simanovskaia, B. K. Spears, R. Tommasini, K. Widmann, A. B. Zylstra, G. W. Collins, O. L. Landen, J. D. Kilkenny, W. W. Hsing, B. J. MacGowan, L. J. Atherton, and M. J. Edwards, Phys. Plasmas **19**, 122702 (2012).
[23]Y. P. Opachich, D. H. Kalantar, A. G. MacPhee, J. P. Holder, J. R. Kimbrough, P. M. Bell, D. K. Bradley, B. Hatch, G. Brienza-Larsen, C. Brown, C. G. Brown, D. Browning, M. Charest, E. L. Dewald, M. Griffin, B. Guidry, M. J. Haugh, D. G. Hicks, D. Homoelle, J. J. Lee, A. J. Mackinnon, A. Mead, N. Palmer, B. H. Perfect, J. S. Ross, C. Silbernagel, and O. Landen, Rev. Sci. Instrum. **83**, 125105 (2012).
[24]R. E. Olson, D. G. Hicks, N. B. Meezan, J. A. Koch, and O. L. Landen, Rev. Sci. Instrum. **83**, 10D310 (2012).
[25]R. P. Drake, *High-Energy-Density Physics: Fundamentals, Inertial Fusion, and Experimental Astrophyiscs* (Springer, Berlin, 2006).
[26]D. Mihalas and B. W. Mihalas, *Foundations of Radiation Hydrodynamics* (New York, Oxford University Press, 1984).
[27]S. Bouquet, R. Teyssier, and J. P. Chieze, ApJS **127**, 245 (2000).
[28]S. Atzeni and J. M. ter Vehn, *The Physics of Inertial Fusion: Beam Plasma Interaction, Hydrodynamics, Hot Dense Matter* (Oxford University Press, USA, 2009).
[29]V. V. Dwarkadas and J. Gruszko, Mon. Not. R. Astron. Soc. **419**, 1515 (2012).